IEEE Photonics Journal
An IEEE Photonics Society Publication

Open Access

Theoretical Investigation of Broadband Frequency Conversion Bridging the Mid-Infrared and Telecom Band Through a Chalcogenide/Sio_2 Hybrid Waveguide

Volume 13, Number 2, April 2021

Yufei Huang
Di Xia
Bin Zhang
Pingyang Zeng
Zelin Yang
Huanjie Cheng
Mingjie Zhang
Ying Zhu
Zhaohui Li

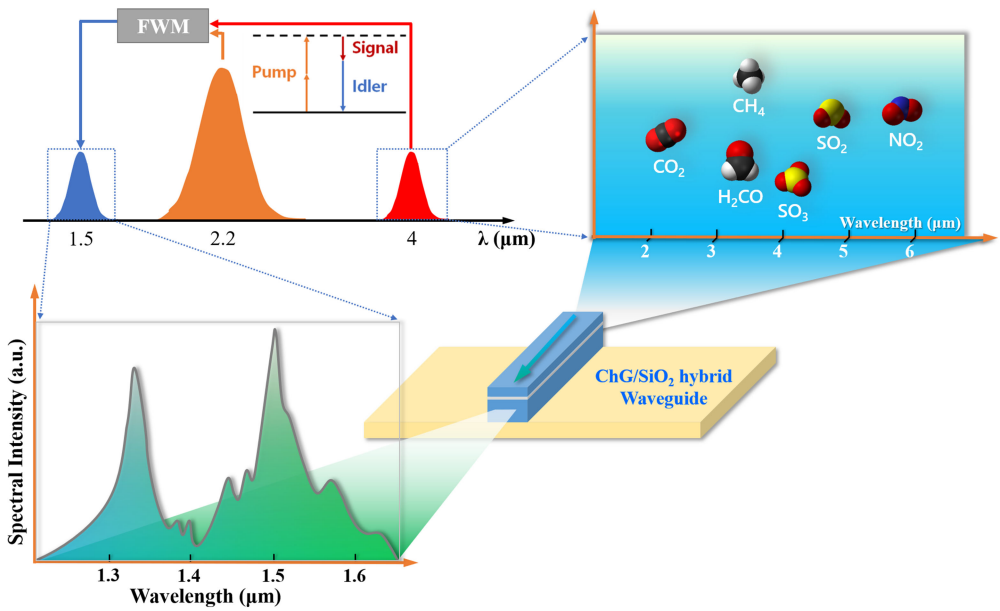

DOI: 10.1109/JPHOT.2021.3065946

Theoretical Investigation of Broadband Frequency Conversion Bridging the Mid-Infrared and Telecom Band Through a Chalcogenide/Sio_2 Hybrid Waveguide

Yufei Huang,[1] Di Xia,[1] Bin Zhang,[1] Pingyang Zeng,[1] Zelin Yang,[1] Huanjie Cheng,[1] Mingjie Zhang,[2] Ying Zhu,[1] and Zhaohui Li[1,3]

[1]State Key Laboratory of Optoelectronic Materials and Technologies, School of Electronics and Information Technology, Sun Yat-sen University, Guangzhou 510275, China
[2]Department of Optoelectronic Engineering, Jinan University, Guangzhou 510632, China
[3]Southern Laboratory of Ocean Science and Engineering (Guangdong, Zhuhai), Zhuhai 519000, China

DOI:10.1109/JPHOT.2021.3065946

Manuscript received January 17, 2021; revised March 8, 2021; accepted March 10, 2021. Date of publication March 15, 2021; date of current version April 7, 2021. This work was supported in part by the Key Project in Broadband Communication and New Network of the Ministry of Science and Technology (MOST) under Grant 2018YFB1801003, in part by the National Key R&D Program of China under Grant 2019YFA0706303, in part by the National Science Foundation of China (NSFC) under Grants 61975242, 62035018, U1701661, U2001601, in part by the Key Project for Science and Technology of Guangzhou City under Grant 201904020048, in part by the Science and Technology Planning Project of Guangdong under Grant Province 2019A1515010774, and in part by the Science Foundation of Guangzhou City under Grant 202002030103. *(Yufei Huang and Di Xia contributed equally to this work.)*
Corresponding author: Bin Zhang (e-mail: zhangbin5@mail.sysu.edu.cn).

Abstract: Capturing the distinctive spectral fingerprints of molecules in the infrared (IR) region is of vital importance in gas detection. However, it is still limited by the resolution, sensitivity and signal to noise ratio of IR detectors. Here, a broadband frequency conversion scheme from the middle IR band (MIR) to the telecom band based on four-wave mixing process is proposed and theoretically investigated, combining the advantages of well-established detectors in the telecom band and unique molecular vibrations in the MIR band. A flat and low dispersion profile is generated in an asymmetric Ge-As-Se/SiO_2 hybrid waveguide, which exhibits four zero-dispersion wavelengths and a dispersion variation of sub-20 ps/nm/km. Furthermore, taking advantage of the high order phase-matching, an ultra-broad 3-dB continuous wavelength conversion bandwidth covering 1454–4521 nm is achieved, which to the best of our knowledge is the widest frequency conversion bandwidth in the chip-scale devices. In addition, a fabrication scheme is proposed for the precise manipulation of dispersion. It holds great potential for practical applications in photonic integrated gas sensing, biomedical diagnostics.

Index Terms: Chalcogenide waveguide, four-wave mixing, frequency conversion, gas detection, integrated optics.

1. Introduction

Highly sensitive and accurate identification of molecules is in great demand in national security, biomedical and industrial engineering applications [1]–[3]. Infrared (IR) spectroscopy is considered

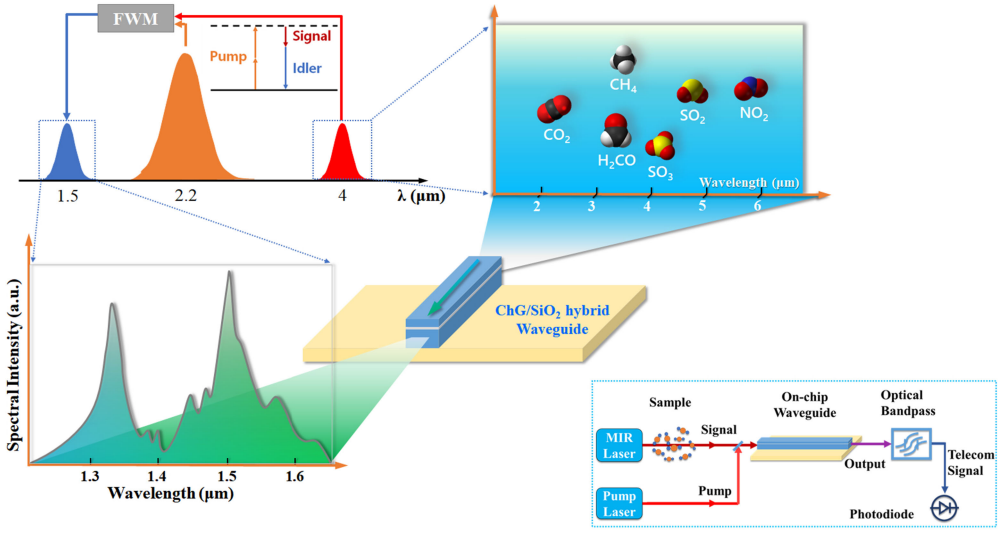

Fig. 1. Schematic of molecular fingerprints frequency conversion from the MIR to telecom band utilizing FWM in an on-chip ChG/SiO_2 hybrid waveguide. Inset: Experimental set-up for gas detection by frequency conversion based on the hybrid waveguide.

the gold standard for molecular structures identification by detecting the distinctive spectral fingerprints of molecules in middle infrared (MIR) region. For example, several trace gases such as CH_4, CO, NO, N_2O, and NO_2 have weak absorption in the near-IR region (NIR, 0.8–1.6 μm) and 100 times stronger absorption peaks in the MIR region (e.g., the stretching frequencies of the molecules containing C-H bonds in the 3–3.7μm region) [4]. Nevertheless, the detectivity is still challenged by low resolution and signal-to-noise ratio of available MIR detectors. Furthermore, MIR spectral systems generally require a low-temperature environment or multi-stage thermoelectric cooling system to suppress dark current noise, which severely impairs their versatility [5], [6].

The frequency conversion scheme based on four-wave mixing process (FWM) has been successfully demonstrated in fibers or on-chip waveguide systems in a wide variety of platforms [6]–[13]. Especially, chip-scale waveguide devices have advantages of small size, low cost, and low power consumption. Such a broadband conversion provides an alternative method for implementing photonic integration of molecular detection. Infrared laser signal carrying the spectral fingerprints of molecule in the MIR band is converted to the telecom band by FWM and detected by the uncooled, high-performance integrated detector in telecom band. The schematic is illustrated in Fig. 1, where the unique combination of the advantages of high-performance devices in the telecom band and the distinctive molecular fingerprints in the MIR band realized in a chip-scale waveguide. However, to achieve a broadband and efficient frequency conversion based on the FWM process in a chip-scale waveguide, it is still challenging to ensure the phase-matching over a large wavelength range.

An ideal integrated nonlinear platform for our target would have both a high optical nonlinearity and a large transparent bandwidth. Chalcogenide glasses (ChGs), which are well-known for their wide transparency window ranging from visible to long-wave IR, high Kerr nonlinearity, low two-photon absorption and ultrafast nonlinearity response, are particularly promising material platforms for photonic integrated nonlinear devices [14], [15].

Among them, $Ge_{11.5}As_{24}Se_{64.5}$ shows excellent film-forming property and negligible refractive index change under intense illumination, which have been verified as a photostable nonlinear candidate in planar waveguides [16]–[19]. Moreover, recent advances in fabrication technology including atomic layer deposition and nano-lithography have realized precise film thickness control and low optical loss. On the other hand, the phase-matching over a large bandwidth is still a problem. Multilayer waveguides structures have been proposed to flatten waveguide dispersion

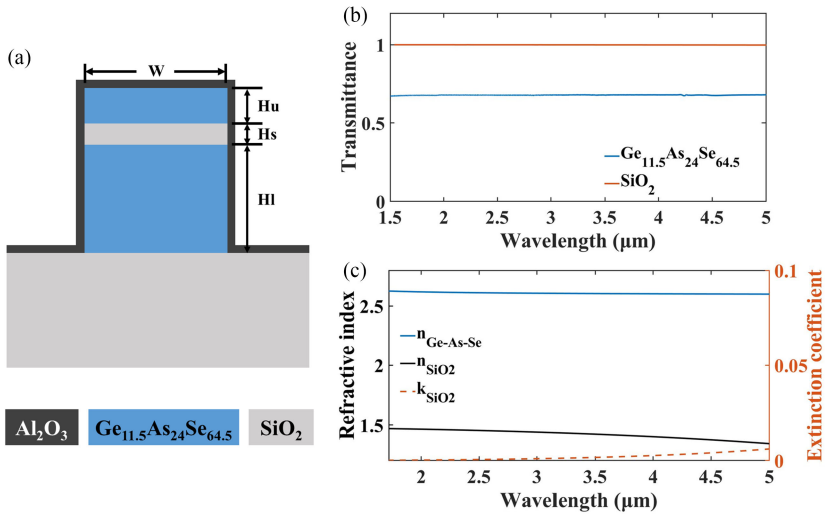

Fig. 2. (a) Cross-section of Ge-As-Se/SiO_2/Ge-As-Se hybrid waveguide. An Al_2O_3 protective layer is deposited on the surface. (b) Optical transmittance and (c) refractive index as well as extinction coefficient of Ge-As-Se bulk and SiO_2 film with a thickness of 1 μm [30], [33].

with multiple zero dispersion wavelengths (ZDWs), which provides flexible material and structure choices [20]–[27]. In AlGaAs waveguide, ultra-high conversion efficiency of -4 dB is realized but the conversion bandwidth is only $\sim$700 nm [28]. Later, the authors showed in simulation that the conversion bandwidth can be improved to an octave (1.1–2.5 μm) [29]. In silicon nanowaveguide, conversion bandwidth over two-thirds of an octave from 1241 nm to 2078 nm is realized [13]. In As_2S_3-SiO_2 double-slot waveguide, a simulated conversion bandwidth of about 1200 nm is realized [30]. However, to date, the conversion bandwidth is still not enough for our target application.

In this work, an asymmetric $Ge_{11.5}As_{24}Se_{64.5}/SiO_2$ hybrid waveguide is proposed and designed to obtain a flat and low dispersion over a large wavelength range. The frequency conversion performance is optimized through utilizing the high-order phase matching and carefully selecting the pump wavelength, as well as waveguide length. A 3 dB continuous frequency conversion covering a 3067 nm or 140 THz bandwidth from MIR to telecom band is achieved in a compact waveguide on chip. In addition, a fabrication process of the hybrid waveguide is proposed to ensure the dispersion tolerance caused by fabrication errors. The proposed scheme might facilitate the on-chip trace gas sensing, biomedical diagnostics, scientific exploration of early diagnosis of cancer.

2. Principle of Dispersion Flattening Based on ChG/SiO_2 Hybrid Waveguide

Achieving phase-matching over a large wavelength bandwidth is of vital importance in realizing our target. Here, a multilayer waveguide structure is proposed to flatten dispersion, whose cross section is demonstrated in Fig. 2(a). We carefully choose $Ge_{11.5}As_{24}Se_{64.5}$ and SiO_2 as the constituents of the hybrid waveguide here. Besides $Ge_{11.5}As_{24}Se_{64.5}$ having high transmittance from visible to MIR [18], the SiO_2 film with a thickness of sub-500 nm also shows good transmission performance in the range of 1.5-5 μm [31], as shown in Fig. 2(b). A high RI contrast between SiO_2 and $Ge_{11.5}As_{24}Se_{64.5}$ shown in Fig. 2(c) provides strong light confinement for enhancing the optical nonlinearity. These attributes are essential for broadband efficient frequency conversion. What's more, considering the aging problem of ChGs when exposed in air, we add a 5-nm layer of Al_2O_3 on the surface as a protective layer [32], [33]. In the following section, we will discuss how to optimize the waveguide parameters to achieve a broadband flattened dispersion profile.

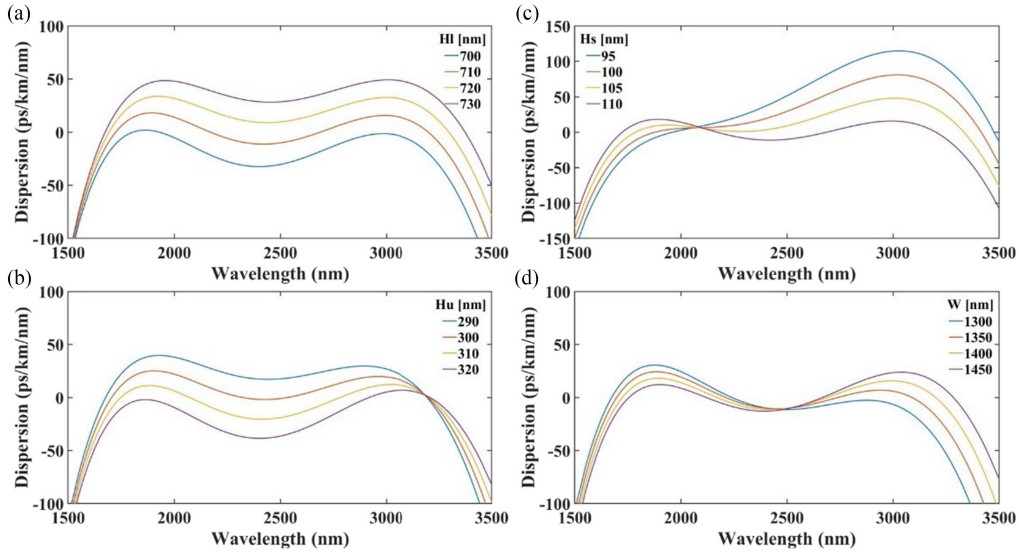

Fig. 3. Dispersion profiles with different structural parameters changed. (a) The lower strip height Hl (W = 1400 nm, Hu = 305 nm, Hs = 110 nm), (b) the upper strip height Hu (W = 1400 nm, Hl = 710 nm, Hs = 110 nm), (c) the slot height Hs (W = 1400 nm, Hu = 305 nm, Hl = 710 nm) and (d) the width W (Hu = 305 nm, Hl = 710 nm, Hs = 110 nm).

2.1. Design and Optimization of Waveguide Structures

Firstly, the effects of each structural parameter on dispersion are systematically investigated. As shown in Fig 2(a), the structural parameters W, Hu, Hs, and Hl stand for the waveguide width, the upper strip height, the slot height, and the lower strip height, respectively. The chromatic dispersion profile of the quasi-TM mode can be calculated through the equation $D = -(\lambda/c) \cdot (d^2 n_{eff}/d\lambda^2)$, where n_{eff} is the effective refractive index. Taking into account material dispersions of $Ge_{11.5}As_{24}Se_{64.5}$, SiO_2 and Al_2O_3 [31], the dispersion value as a function of wavelength is obtained using finite element method. As is shown in Fig. 3(a), when increasing the lower strip height Hl, the overall dispersion profile is moved from normal to anomalous regime gradually. In contrast, the dispersion is moved from anomalous to normal regime as the Hu increases, as shown in Fig. 3(b). The profile flips with respect to around 2.1 μm, reflecting more sensitivity to Hs at long wavelengths than that at short ones, shown in Fig 3(c). At the same time, the dispersion profile flips with respect to around 2.5 μm when W increases, as indicated in Fig. 3(d). Following the trend of the shape and bandwidth of dispersion profile on these parameters, a low and flat dispersion profile can be finely tailored by adjusting these structural parameters.

2.2. Dispersion Profile and Nonlinear Characteristics of the Optimized Waveguide

From above, a flat and low dispersion profile with saddle-shape of the hybrid waveguide can be achieved by setting the structural parameters as W = 1400 nm, Hu = 305 nm, Hl = 710 nm, Hs = 110 nm. The four ZDWs are located at 1720 nm, 2170 nm, 2690 nm and 3200 nm, as shown in Fig. 4(a). The quasi-transverse-magnetic (quasi-TM) mode distributions at the wavelengths of 1600, 2200, 2800 and 3400 nm are also demonstrated in Fig 4(a). It shows that a great part of the optical field for the quasi-TM modes gradually shifts from the lower $Ge_{11.5}As_{24}Se_{64.5}$ layer to the SiO_2 layer as the wavelength increases. At shorter wavelength, most part of the fundamental quasi-TM mode is confined in lower $Ge_{11.5}As_{24}Se_{64.5}$ layer, thus, the total dispersion is mainly determined by material dispersion in this wavelength range. In the middle wavelength range, optical power enters the slot layer (mode transition), which provides additional normal dispersion and results in four ZDWs, generating a saddle-shaped dispersion profile [20]. At longer wavelengths,

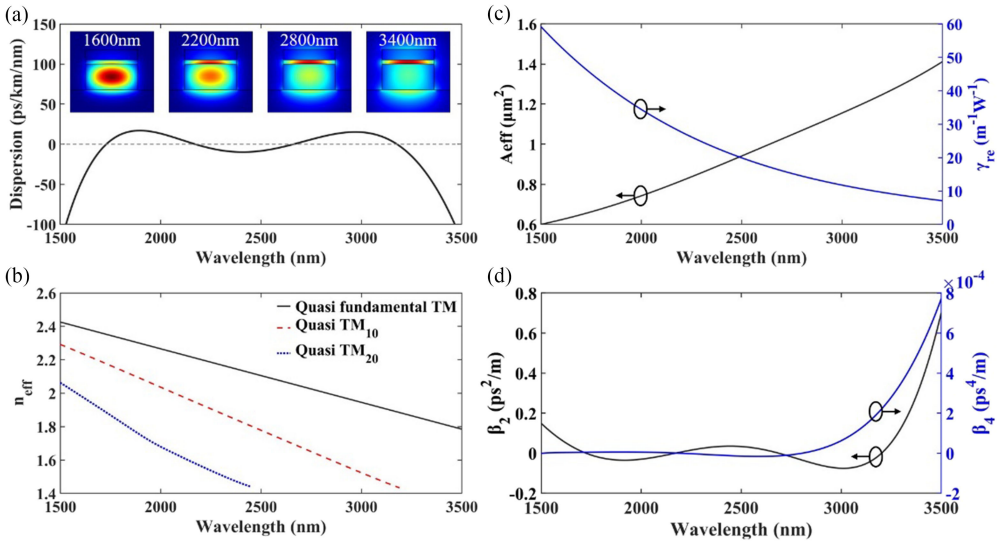

Fig. 4. (a) Dispersion profile with four ZWDs and optical field distributions of the quasi-TM mode at different wavelengths, (b) Effective refractive indices of higher-order modes and fundamental quasi-TM mode versus wavelength, (c) Calculated A_{eff} and γ of the optimized waveguide versus wavelength, (d) Calculated second- and fourth-order dispersion coefficient profile of the optimized waveguide.

the total dispersion is dominated by waveguide dispersion and only a small portion of power enters the substrate and cladding layer. This effect could load the low and flat dispersion by tailoring structural parameters.

Besides, the waveguide structure is quite small so that it only supports two higher-order modes at the TM polarization, i.e., TM_{10} and TM_{20} modes. Fig. 4(b) shows the effective refractive indices of higher-order modes and fundamental quasi-TM mode. The cut-off wavelengths of higher-order modes are below 3200 nm.

Moreover, the effective mode area and nonlinear coefficient play a vital role in frequency conversion based on FWM. The effective mode area (A_{eff}) and the real part of nonlinear coefficient (γ) of the waveguide are [35], [36]:

$$A_{\text{eff}} = \frac{\left|\iint_{-\infty}^{+\infty} (\boldsymbol{e} \times \boldsymbol{h}^*) \cdot \hat{z} dxdy\right|^2}{\iint_{-\infty}^{+\infty} \left|(\boldsymbol{e} \times \boldsymbol{h}^*) \cdot \hat{z}\right|^2 dxdy} \tag{1}$$

$$\gamma = k\left(\frac{\varepsilon_0}{\mu_0}\right) \frac{\iint_{-\infty}^{+\infty} n^2(\mathrm{x}, \mathrm{y})\, n_2(x, y)\left[2|\boldsymbol{e}|^4 + \left|\boldsymbol{e}^2\right|^2\right] dxdy}{3\left|\iint_{-\infty}^{+\infty} (\boldsymbol{e} \times \boldsymbol{h}^*) \cdot \hat{z} dxdy\right|^2} \tag{2}$$

where $\boldsymbol{e}$ and $\boldsymbol{h}$ is the electric field vector and magnetic field vector respectively, n_2 is the Kerr index of materials (in this study, we take $n_2 = 9 \times 10^{-18}$ m^2/W for $Ge_{11.5}As_{24}Se_{64.5}$ [18]), and λ is wavelength. The A_{eff} and γ of the optimized waveguide as a function of wavelength are depicted in Fig. 4(c). The A_{eff} is increased as wavelength increases, which is less than 1.4 μm^2 in the wavelength range from 1.5 μm to 3.5 μm. On the other hand, the γ is gradually decreased as wavelength increases. The maximum γ is as large as 59 W^{-1}m^{-1} at 1.5 μm, which is about 2.8 $\times$ 10^4 times higher than that of the single-mode silica fiber [35].

3. High-Order Phase-Matching Enabled Broadband Frequency Conversion

In order to obtain higher frequency conversion efficiency, the effects of dispersion and nonlinearity on the phase matching is studied. For degenerate FWM, the phase mismatch can be expressed

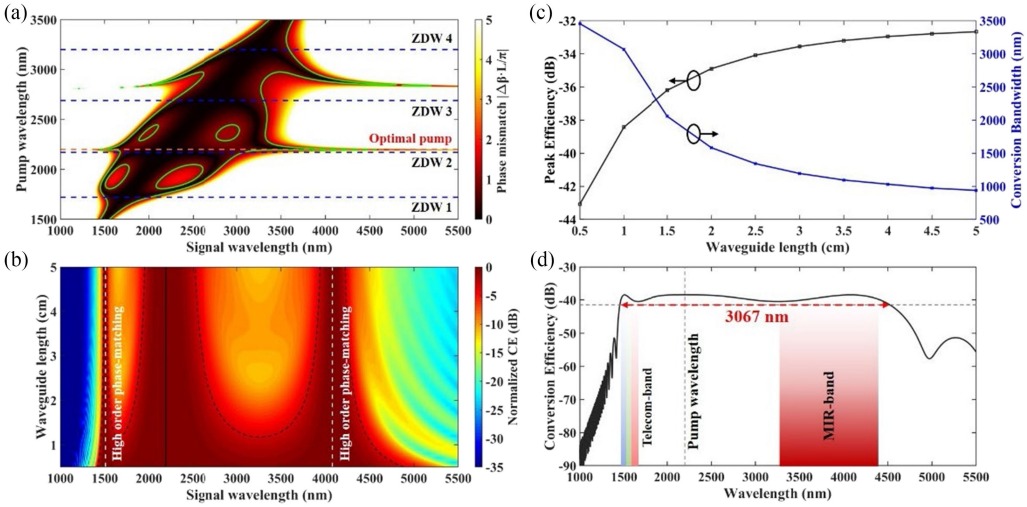

Fig. 5. (a) Calculated phase mismatch $|\Delta\beta \cdot L/\pi|$ for different pump and signal wavelength setting for the $Ge_{11.5}As_{24}Se_{64.5}/SiO_2$ hybrid waveguide with a length of 1.5 cm and (b)calculated normalized conversion efficiency as a function of signal wavelength for different waveguide length. The black line and white dash lines show the pump wavelength and the high-order phase-matched wavelengths, (c) Calculated peak conversion efficiency and 3 dB conversion bandwidth as a function of the waveguide length and (d) FWM conversion efficiency as a function of signal wavelength, the 3 dB continuous conversion bandwidth reaches 3067 nm (1454–4521 nm), and the MIR-band signal (3357-4380 nm) can be transferred to the telecom band.

as $\Delta k = \Delta\beta + 2\gamma P_p$, where $\Delta\beta = 2\beta_p - \beta_s - \beta_i$ is the linear phase mismatch between pump, signal, and idler waves, and β_p, β_s and β_i are the propagation constants for pump, signal and idler, respectively. $2\gamma P_p$ is the nonlinear phase term induced by self-phase modulation (SPM) and cross-phase modulation (XPM). The $\Delta\beta$ is related to the dispersion profile by using the following relation [37]:

$$\Delta\beta = \beta_2\ (\omega_p)\,\Omega^2 + \frac{1}{12}\beta_4\,(\omega_p)\,\Omega^4 \tag{3}$$

where β_2 and β_4 are second- and fourth-order dispersion parameters at pump wavelength, respectively, and Ω is the angular frequency separation between pump and signal. Operating in the undepleted pump regime [38], the FWM conversion efficiency can be calculated by $\gamma^2 P_p{}^2 L_{eff}{}^2 \eta$, where $L_{eff} = (1 - e^{-\alpha L})/\alpha$ is the effective length of the waveguide (α: the loss per unit length and 3 dB/cm [6] is used in this calculation, L: the waveguide length). The phase matching factor η can be expressed as:

$$\eta = \alpha^2 \left(1 + 4e^{-\alpha L}\frac{\sin^2(\Delta\beta L/2)}{\left(1-e^{-\alpha L}\right)^2}\right) / \left(\alpha^2 + \Delta\beta^2\right). \tag{4}$$

As is shown in Fig. 4(d), the calculated β_2 and β_4 dispersion profiles express different signs in three wavelength ranges where a discrete frequency conversion based on high-order phase-matching can be potentially achieved with a large pump-signal frequency detuning [39], [40]. However, the discrete conversion is generally narrowband and thus limits the practical applications. Therefore, in order to realize broadband continuous frequency conversion, the effects of pump wavelength and waveguide length on the phase matching should be studied [28]. Fig. 5(a) shows the simulated phase-mismatch ($|\Delta\beta \cdot L/\pi|$) for different pump and signal wavelengths setting in the $Ge_{11.5}As_{24}Se_{64.5}/SiO_2$ hybrid waveguide with an optimized cross-section parameter (W = 1400 nm, Hu = 305 nm, Hl = 710 nm, Hs = 110 nm) and a length of 1 cm. The green contour line indicates the near phase-matched condition ($|\Delta\beta \cdot L/\pi| = 1$), where the conversion efficiency is half that of the perfect phase-matched case, and the blue dash lines denote four zero-dispersion

wavelengths (ZDW1-ZDW4, numbered from short wavelength to long wavelength). When pumping at the red-detuned of the second ZDW (2200 nm, the red dash line in Fig. 5(a)), the fundamental conversion band can be merged with high-order phase-matching bands to realize an ultra-broad continuous conversion band. There are CW fiber laser sources below 2.21 μm that can provide enough pump power of $>$60 mW, considering a 3 dB fiber-to-chip coupling loss [41], [42].

Fig. 5(b) shows the simulated normalized conversion efficiency evolution as the waveguide length increases when the waveguide is pumped at 2200 nm. The black line and two white dash lines correspond to the pump wavelength and high-order phase-matched wavelengths, respectively. The black dash contour indicates a normalized conversion efficiency of -3 dB. As shown in Fig. 5(c), the conversion efficiency increases with the waveguide length due to the enhanced interaction length, while the 3 dB conversion bandwidth shows the opposite trend, resulting from the accumulation of phase mismatch between signal and pump in the waveguide. Note that the conversion bandwidth exhibits a sharp decline at 1.5 cm, because the high-order phase-matching bands are separate from the fundamental band. It is shown in Fig 5(b) that the continuous conversion band appears as long as the waveguide length does not exceed 1 cm. Thus, the waveguide length of 1 cm is selected for the next calculation of conversion efficiency in this work.

Considering both damage threshold of materials and available pump power (with 3 dB fiber-to-chip coupling loss), a pump power of 60 mW is used. Fig. 5(d) shows the conversion efficiency as a function of signal wavelength when the waveguide is pumped at 2200 nm with a power of 60 mW. The 3 dB continuous conversion bandwidth can be extended to 3067 nm (from 1454 to 4521 nm), i.e., 140 THz, with a peak conversion efficiency of -38.43 dB. Correspondingly, the performance of frequency conversion between MIR band and telecom band is also demonstrated in Fig. 5(d). Signal at MIR band (covering 3357-4380 nm wavelength range) can be transferred to the telecom band (covering 1460-1625 nm wavelength range). Moreover, the conversion efficiency is flat within the operating wavelength range. With high detectivity of telecom-band detectors, this conversion efficiency level creates enough power for detection. Compared with the previous reports [37], [39], [40], [43], [44], our result achieves the widest frequency conversion bandwidth in a monolithic integrated waveguide.

4. Analysis of Fabrication Tolerance

Practically, the overall dispersion shape and bandwidth are also affected by the changes of the slot height from fabrication errors. Accordingly, we propose a fabrication scheme for the hybrid waveguide, as shown in Fig. 6, to further improve the fabrication tolerance for dispersion engineering. Firstly, the lower $Ge_{11.5}As_{24}Se_{64.5}$ film is deposited via thermal evaporation onto a silicon wafer with a 300μm SiO_2 layer (TOX). Then a thin SiO_2 layer is deposited on it by ALD. Next, the upper $Ge_{11.5}As_{24}Se_{64.5}$ layer is deposited using similar parameters of the lower layer. The thicknesses of the $Ge_{11.5}As_{24}Se_{64.5}$ and SiO_2 films are accurately measured by AFM, respectively. After films deposition, the photoresist film (PR) is spin-coated onto the wafer and the waveguide is patterned by electron-beam lithography (EBL) and etched in an inductively coupled plasma (ICP) reactive ion etcher with CHF_3 gas [45]. Note, the $Ge_{11.5}As_{24}Se_{64.5}$ and SiO_2 can be etched by CHF_3 simultaneously. Finally, a 5-nm protective Al_2O_3 layer is deposited on the surface of our sample by ALD. Enabled by state-of-the-art film deposition and nano-lithography techniques, the slot film thickness can be controlled within 2 nm accuracy while the slab layer thickness and waveguide width controlled within 10 nm accuracy.

To analyze the fabrication tolerance, we randomly change the structural parameters within the aforementioned accuracy range to simulate practical fabrication error. Six different structures are listed in Table 1. Fig. 7 demonstrates the dispersion profiles of these waveguide structures. The overall dispersion variation is about $\pm$25 ps/nm/km. The peak efficiencies, conversion bandwidths and corresponding simulation parameters of these six waveguides are also shown in Table 1. Note that all the results are simulated with a pump power of 60 mW. As we can see, some bandwidths are narrowed to several hundred nanometers because the high-order phase-matching bands are separate from the fundamental conversion band. However, we can still achieve our

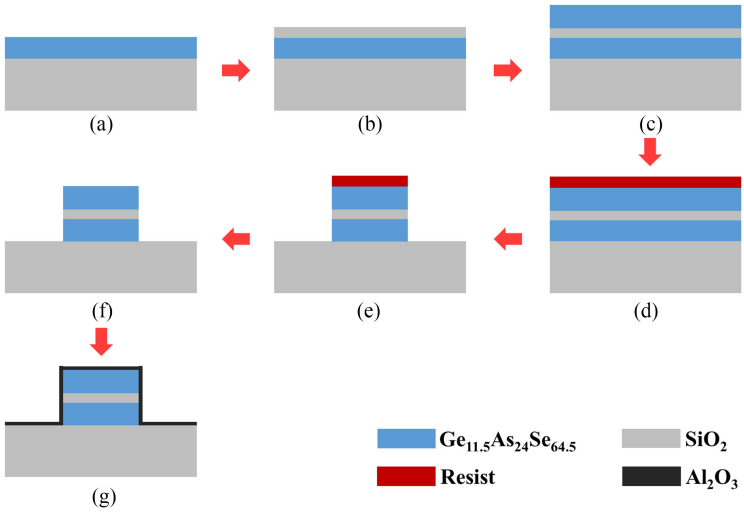

Fig. 6. A suggested waveguide fabrication process. (a) Thermal evaporation of the lower ChG film on TOX wafer, (b) ALD of the SiO_2 film, (c) Thermal evaporation of the upper ChG film, (d) Spin-coating of the PR layer, (e) EBL and ICP etching of the waveguide and (f) Removing of PR film, (g) ALD of the Al_2O_3 protective layer.

TABLE 1
Parameters Setting and Conversion Bandwidth for Different Waveguide Structures

No.	W (nm)	Hu (nm)	Hl (nm)	Hs (nm)	λ_p (nm)	L (cm)	Peak efficiency (dB)	3dB bandwidth (nm)
1	1404	304	709	108	2150	1	-37.96	2099
2	1397	304	707	108	2180	1	-38.24	1901
3	1406	311	712	110	2220	0.8	-40.02	1000
4	1407	297	703	108	2150	1	-37.96	2964
5	1403	315	716	112	2260	0.8	-40.4	829
6	1407	303	703	109	2210	0.8	-39.93	838

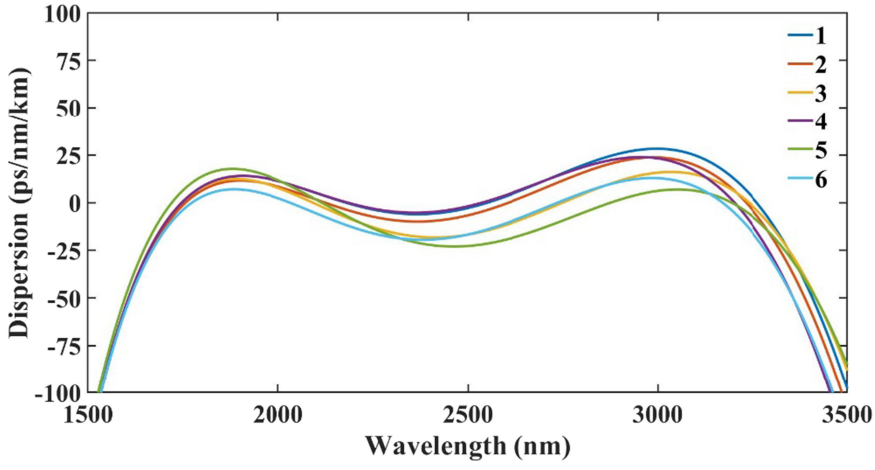

Fig. 7. Dispersion profiles of six different waveguides corresponding to Table 1.

target at bridging NIR and MIR-band through tuning pump wavelength, which simultaneously tune the positions of the high-order phase-matching bands. The peak efficiency ranges from −37.96 dB to −40.4 dB, which is acceptable since photodetectors operated in telecom-band have relatively high detectivity. Based on the above analysis, we can emphasize that the dispersion of the hybrid waveguide has a good fabrication tolerance. This indicates that achieving broadband frequency conversion should consider several key elements altogether, including the effective nonlinearity and dispersion of the waveguides, as well as accurate fabrication process allowing precise control of dispersion and low optical loss.

5. Conclusion

A Ge-As-Se/SiO_2 hybrid waveguide with a low and flat dispersion has been proposed for broadband frequency conversion. A flat dispersion with four ZDWs across 1530 nm with a total variation of 10 ps/nm/km is achieved by fine dispersion engineering. A 3 dB conversion bandwidth of 3067 nm, i.e., 140 THz, with peak conversion efficiency of −38.43 dB is achieved when pumped at 2200 nm with a power of 60 mW. A fabrication scheme is proposed for the precise control of dispersion. The results highlight that the photonic chip-based frequency conversion based on FWM has potential in detecting fingerprints of the molecules.

Acknowledgment

The authors wish to thank the anonymous reviewers for their valuable suggestions.

References

[1] M. Yilmaz *et al.*, "Nanostructured organic semiconductor films for molecular detection with surface-enhanced raman spectroscopy," *Nature Mater.*, vol. 16, pp. 918–924, 2017.
[2] H. Hu *et al.*, "Far-field nanoscale infrared spectroscopy of vibrational fingerprints of molecules with graphene plasmons," *Nature Commun.*, vol. 7, 2016, Art. no. 12334.
[3] J. O. Arroyo and P. Kukura, "Non-fluorescent schemes for single-molecule detection, imaging and spectroscopy," *Nature Photon.*, vol. 10, pp. 11–17, 2016.
[4] M. A. Butt, S. N. Khonina, and N. L. Kazanskiy, "Silicon on silicon dioxide slot waveguide evanescent field gas absorption sensor," *J. Mod. Opt.*, vol. 65, pp. 174–178, 2017.
[5] S. M. Sze and K. K. Ng, *Physics of Semiconductor Devices*. Hoboken, NJ, USA: Wiley, 2006.
[6] K. Guo *et al.*, "Broadband wavelength conversion in a silicon vertical-dual-slot waveguide," *Opt. Exp.*, vol. 25, pp. 32964–32971, 2017.
[7] X. Lu *et al.*, "Milliwatt-threshold visible–telecom optical parametric oscillation using silicon nanophotonics," *Optica*, vol. 6, pp. 1535–1541, 2019.
[8] S. Zlatanovic *et al.*, "Mid-infrared wavelength conversion in silicon waveguides using ultracompact telecom-band-derived pump source," *Nature Photon.*, vol. 4, pp. 561–564, 2010.
[9] X. Lu *et al.*, "Efficient telecom-to-visible spectral translation through ultralow power nonlinear nanophotonics," *Nature Photon.*, vol. 13, pp. 593–601, 2019.
[10] R. Jiang *et al.*, "Continuous-wave band translation between the near-infrared and visible spectral ranges," *J. Lightw. Technol.*, vol. 25, pp. 58–66, 2007.
[11] S. Xing *et al.*, "Mid-infrared continuous-wave parametric amplification in chalcogenide microstructured fibers," *Optica*, vol. 4, pp. 643–648, 2017.
[12] T. Huang, J. Liao, S. Fu, M. Tang, P. Shum, and D. Liu, "Slot spiral silicon photonic crystal fiber with property of both high birefringence and high nonlinearity," *IEEE Photon. J.*, vol. 6, no. 3, Jun. 2014, Art. no. 2200807.
[13] A. C. Turner-Foster, M. A. Foster, R. Salem, A. L. Gaeta, and M. Lipson, "Frequency conversion over two-thirds of an octave in silicon nanowaveguides," *Opt. Exp.*, vol. 18, pp. 1904–1908, 2010.
[14] B. J. Eggleton, B. Luther-Davies, and K. Richardson, "Chalcogenide photonics," *Nature Photon.*, vol. 5, pp. 141–148, 2011.
[15] Y. Yu *et al.*, "Mid-infrared supercontinuum generation in chalcogenides," *Opt. Mater. Exp.*, vol. 3, pp. 1075–1086, 2013.
[16] Y. Yu *et al.*, "A broadband, quasi-continuous, mid-infrared supercontinuum generated in a chalcogenide glass waveguide," *Laser Photon. Rev.*, vol. 8, pp. 792–798, 2014.
[17] D. Bulla, R. Wang, A. Prasad, A. V. Rode, S. Madden, and B. Luther-Davies, "On the properties and stability of thermally evaporated Ge–As–Se thin films," *Appl. Phys. A: Mater. Sci. Process.*, vol. 96, pp. 615–625, 2009.
[18] B. Zhang *et al.*, "High brightness 2.2-12 μm mid-infrared supercontinuum generation in a nontoxic chalcogenide step-index fiber," *J. Amer. Ceram. Soc.*, vol. 99, pp. 2565–2568, 2016.
[19] X. Gai, S. Madden, D.-Y. Choi, D. Bulla, and B. Luther-Davies, "Dispersion engineered $Ge_{11.5}As_{24}Se_{64.5}$ nanowires with a nonlinear parameter of 136$W^{-1}m^{-1}$ at 1550 nm," *Opt. Exp.*, vol. 18, pp. 18866–18874, 2010.

[20] L. Zhang, Q. Lin, Y. Yue, Y. Yan, R. G. Beausoleil, and A. E. Willner, "Silicon waveguide with four zero-dispersion wavelengths and its application in on-chip octave-spanning supercontinuum generation," *Opt. Exp.*, vol. 20, pp. 1685–1690, 2012.
[21] Y. Guo *et al.*, "Bilayer dispersion-flattened waveguides with four zero-dispersion wavelengths," *Opt. Lett.*, vol. 41, pp. 4939–4942, 2016.
[22] Z. Jafari, L. Zhang, A. M. Agarwal, L. C. Kimerling, J. Michel, and A. Zarifkar, "Parameter space exploration in dispersion engineering of multilayer silicon waveguides from near-infrared to mid-infrared," *J. Lightw. Technol.*, vol. 34, pp. 3696–3702, 2016.
[23] Y. Guo *et al.*, "Ultra-flat dispersion in an integrated waveguide with five and six zero-dispersion wavelengths for mid-infrared photonics," *Photon. Res.*, vol. 7, pp. 1279–1286, 2019.
[24] A. S. Kowligy *et al.*, "Tunable mid-infrared generation via wide-band four-wave mixing in silicon nitride waveguides," *Opt. Lett.*, vol. 43, pp. 4220–4223, 2018.
[25] Z. Hui, M. Yang, M. Zhang, X. Zeng, J. Gong, and A.-H. Soliman, "Design of a dispersion-engineered broadband $Ge_{11.5}As_{24}Se_{64.5}$-$Si_3N_4$ strip–slot hybrid waveguide with giant and flat dispersion over 350 nm for on-chip photonic networks," *Opt. Commun.*, vol. 451, pp. 323–332, 2019.
[26] C. Koos *et al.*, "All-optical high-speed signal processing with silicon–organic hybrid slot waveguides," *Nature Photon.*, vol. 3, pp. 216–219, 2009.
[27] Z. Hui, L. Zhang, L. Wang, and W. Zhang, "Dispersion engineering of a As_2Se_3-based strip/slot hybrid waveguide for mid-infrared broadband wavelength conversion," *Mod. Phys. Lett. B*, vol. 30, no. 28, 2016, Art. no. 1650336.
[28] M. Pu *et al.*, "Ultra-efficient and broadband nonlinear AlGaAs-on-insulator chip for low-power optical signal processing," *Laser Photon. Rev.*, vol. 12, 2018, Art. no. 1800111.
[29] Y. Liu, M. Galili, K. Yvind, L. K. Oxenløwe, H. Hu, and M. Pu, "High-order phase-matching enabled octave-bandwidth four-wave mixing in AlGaAs-on-insulator waveguides," in *CLEO: Applications and Technology*, San Jose, CA, USA: Optical Society of America, 2019, pp. 2.
[30] Y. Wang *et al.*, "Broadband and transparent wavelength conversion based on dispersion-flattened double-slot waveguide," *Appl. Opt.*, vol. 54, pp. 7520–7524, 2015.
[31] J. Kischkat *et al.*, "Mid-infrared optical properties of thin films of aluminum oxide, titanium dioxide, silicon dioxide, aluminum nitride, and silicon nitride," *Appl. Opt.*, vol. 51, pp. 6789–6798, 2012.
[32] P. F. Carcia, R. S. McLean, M. D. Groner, A. A. Dameron, and S. M. George, "Gas diffusion ultrabarriers on polymer substrates using Al_2O_3 atomic layer deposition and SiN plasma-enhanced chemical vapor deposition," *J. Appl. Phys.*, vol. 106, 2009, Art. no. 023533.
[33] X. Wang, Y. Z. Cao, C. Yang, L. Yan, and Y. Li, "Vanadium dioxide film protected with an atomic-layer-deposited Al_2O_3 thin film," *J. Vac. Sci. Technol. A*, vol. 34, 2016, Art. no. 01A106.
[34] B. Zhang *et al.*, "Low loss, high NA chalcogenide glass fibers for broadband mid-infrared supercontinuum generation," *J. Amer. Ceram. Soc.*, vol. 98, pp. 1389–1392, 2015.
[35] G. P. Agrawal, *Nonlinear Fiber Optics*. 5th ed. San Diego, CA, USA: Academic, 2012.
[36] S. Afshar V and T. M. Monro, "A full vectorial model for pulse propagation in emerging waveguides with subwavelength structures part I: Kerr nonlinearity," *Opt. Exp.*, vol. 17, pp. 2298–2318, 2009.
[37] M. A. Foster, A. C. Turner, R. Salem, M. Lipson, and A. L. Gaeta, "Broad-band continuous-wave parametric wavelength conversion in silicon nanowaveguides," *Opt. Exp.*, vol. 15, pp. 12949–12958, 2007.
[38] R. Tkach, A. Chraplyvy, F. Forghieri, A. Gnauck, and R. Derosier, "Four-photon mixing and high-speed WDM systems," *J. Lightw. Technol.*, vol. 13, pp. 841–849, 1995.
[39] D. Lyu, Q. Jin, and S. Gao, "Design of mid-infrared nonlinear silicon–germanium waveguides for broadband/discrete-band wavelength conversion," *J. Opt. Soc. Amer. B*, vol. 35, pp. 741–751, 2018.
[40] Y. Huang *et al.*, "Electrical signal-to-noise ratio improvement in indirect detection of mid-IR signals by wavelength conversion in silicon-on-sapphire waveguides," *Appl. Phys. Lett.*, vol. 99, 2011, Art. no. 181122.
[41] J. Li *et al.*, "Wide wavelength selectable all-fiber thulium doped fiber laser between 1925 nm and 2200 nm," *Opt. Exp.*, vol. 22, pp. 5387–5399, 2014.
[42] S. O. Antipov *et al.*, "Holmium fibre laser emitting at 2.21 μm," *Quantum Electron.*, vol. 43, pp. 603–604, 2013.
[43] X. Liu, B. Kuyken, G. Roelkens, R. Baets, R. M. Osgood, and W. M. J. Green, "Bridging the mid-infrared-to-telecom gap with silicon nanophotonic spectral translation," *Nature Photon.*, vol. 6, pp. 667–671, 2012.
[44] E.-K. Tien *et al.*, "Discrete parametric band conversion in silicon for mid-infrared applications," *Opt. Exp.*, vol. 18, pp. 21981–21989, 2010.
[45] Z. Chen *et al.*, "Optical, mechanical and thermal characterizations of suspended chalcogenide glass microdisk membrane," *Opt. Exp.*, vol. 27, pp. 15918–15925, 2019.